PAPER

Linear analysis of electrostatic waves in the lunar wake plasma

To cite this article: T Sreeraj *et al* 2020 *Phys. Scr.* **95** 045610

IOP Publishing Physica Scripta

Phys. Scr. 95 (2020) 045610 (11pp) https://doi.org/10.1088/1402-4896/ab7142

Linear analysis of electrostatic waves in the lunar wake plasma

T Sreeraj, S V Singh and G S Lakhina

Indian Institute of Geomagnetism, New Panvel (West), Navi Mumbai, Maharashtra-410218, India

E-mail: sreerajt90@gmail.com

Received 31 October 2019, revised 16 January 2020
Accepted for publication 29 January 2020
Published 20 February 2020

Abstract

Propagation characteristics of electrostatic electron and ion cyclotron waves, ion- and electron-acoustic waves in a four-component magnetized plasma comprising of protons, doubly charged Helium ions, beam electrons and superthermal electrons following a kappa distribution are presented. The model supports 12 plasma modes: two electron cyclotron (modes 1 and 12), two electron acoustic (modes 2 and 11), two fast ion acoustic (modes 3 and 10), two slow ion acoustic (modes 4 and 9), two proton cyclotron (modes 5 and 8) and two Helium cyclotron (modes 6 and 7). At parallel propagation, with increase in electron beam speed, mode 11 first merges with slow ion acoustic mode 4 and then with fast ion acoustic mode 3 and drives them unstable. For oblique propagation and without the electron streaming, coupling of various plasma modes occurs and it weakens with increase in the angle of propagation. Further, for oblique propagation with finite electron beam velocity, merging as well as coupling of various plasma modes are observed. Growth rates as well as wave numbers of the excited slow and fast ion acoustic modes are much smaller in magnetized plasma than in an unmagnetized one. The results are relevant to observations of electrostatic waves in the lunar wake.

Keywords: plasma waves, Nonthermal distribution, magnetized plasmas, plasma properties

(Some figures may appear in colour only in the online journal)

1. Introduction

The wake region of moon, commonly called as lunar wake, is an interesting natural laboratory to study various types of plasma waves and related phenomenon. This wake region is formed by the interaction of moon with the solar wind impinging on its surface [1–3]. Early studies of moon were conducted by Dolginov *et al* [4, 5] using Luna 1 and Luna 2 satellites. They concluded that either the magnetic field of the Moon is too weak to be observed, else it is not present at all. Analysis of data from IMP-1 (Explorer 18) by Ness [6] showed that the approximate length of lunar wake region can go up-to 150 lunar radii. For typical solar wind parameters, Michel [7] deduced that the approximate length may extend only up-to 5–10 R_m, where $R_m = 1720$ km, is the lunar radius.

Bosqued *et al* [8] have reported that a structured lunar plasma umbra (or plasma cavity) can be seen in the downstream of the Moon at $\sim 6R_m$. Electron and ion densities decrease to a value of 0.5 cm^{-3} near to the center of the optical umbra. Bale *et al* [9] have reported the presence of ion acoustic waves, Langmuir waves and beam modes in the wake region of the Moon using the data from Wind satellite. Farrell *et al* [10] have demonstrated that ion beam drives the electrostatic waves unstable and thereby generating broad-band electrostatic noise[11]. Hashimoto *et al* [12] have shown that intense waves in frequency range of 10–20 kHz are Langmuir waves enhanced at local plasma frequency. Besides, there have been studies of nonlinear electrostatic waves in solar wind-lunar wake plasmas [13–16](see Lakhina *et al* [17] for an extensive review). Advancement in technology has revived the interest in investigation of moon with various satellite missions being planned/underway [18–22].

With the help of data from spacecraft P1 of the new ARTEMIS (Acceleration, Reconnection, Turbulence, and Electrodynamics of the Moons Interaction with the Sun) mission, Wiehle *et al* [23] showed the presence of basic

MHD modes, i.e., fast, Alfvén and slow modes in the lunar wake region. It also measured the electrostatic oscillations closely correlated with counter streaming electron beams in the wake [24]. Halekas *et al* [24] showed that wake potential driven by the refilling process filters and accelerates both ions and electrons thereby generating numerous instabilities. In a comprehensive study, Tao *et al* [25] reported the existence of electrostatic waves in the lunar wake. Furthermore, by 1-D Vlasov simulation, they have speculated that observed electrostatic waves are the electron beam mode branch, which falls in the frequency range of (0.1-0.4)f_{pe}, where f_{pe} is the electron plasma frequency. Through a nonlinear analysis of four component plasma modeled by hot protons, hot heavier ions (α-particles, He^{++}), electron beam, and superthermal electrons following kappa distribution, Rubia *et al* [26] have explained the low frequency part ($<0.01f_{pe}$) of observed spectrum of electrostatic waves in lunar wake [25]. Sreeraj *et al* [27] have undertaken linear analysis of the model proposed by Rubia *et al* [26] and have shown that fast and slow ion acoustic modes are driven unstable when a finite electron beam is introduced into the system. These are electron beam driven fast and slow ion-acoustic modes. The frequency corresponding to the maximum growth rate of these modes agree with the observed high and low frequency waves reported by Tao *et al* [25].

In space plasmas, particle distributions often exhibit the long tail of high energy particles. These distributions depart from Maxwellian and are known as nonthermal distributions. One such distribution is described by kappa distribution [28]. Vasyliunas [29] used it to fit the electron number data in the magnetosphere by OGO 1 (Orbiting Geophysical Observatory) and OGO 3 satellites. In literature it is also known as superthermal or suprathermal distribution. Ever since, it has been used by many researchers to study various phenomena in space and solar plasmas ([30, 31] and references therein). The particles having kappa distributions have also been observed in lunar wake plasma and can contribute to lunar wake dynamics [32–35]. Halekas *et al* [33] have shown that morphology of the lunar wake is best reproduced only when the kappa distribution function is used for electrons. Plasma refilling process is seen to be affected if the electron distribution function is modeled by kappa rather than Maxwellian[35]. Tao *et al* [25] developed a simulation model based on kappa distribution of electrons to explain the observed electrostatic waves in the lunar wake plasma.

In this paper, we extend the theoretical model discussed in Rubia *et al* [26] and Sreeraj *et al* [27] to include the effects of ambient magnetic field. The motivation to consider superthermal electrons for the study of electrostatic waves in the lunar wake has come from Tao *et al* [25]. The purpose of the present study is to delineate coupling and generation of electrostatic waves by electron beam. The linear study allows us to understand the characteristics of normal modes present in the system. However, one can carry out nonlinear analysis using small amplitude or Sagdeev pseudo-potential methods to investigate the quasi-stationary structures. This is beyond the scope of the present study. In the description of plasmas by magnetohydrodynamics (MHD) or kinetic theory, the scale lengths such as Larmor radius or Debye length play important role. In fluid theory, resonant wave particle interaction and Landau damping effects are neglected. The present work deals with non-resonant instability, which can be studied by using MHD equations. Further, in magnetized plasmas, fluid approach can be used when Larmor radius is larger than the Debye length [36]. In section 2, the theoretical model to describe the Lunar wake plasma is discussed and general dispersion relation is derived. The effect of variation of electron beam velocity and propagation angle on the dispersion characteristics of the waves is carried out section 3. The results are discussed and concluded in section 4.

2. Theoretical model

Lunar wake plasma is modeled by a homogeneous, collisionless, and magnetized four-component plasma comprising of fluid protons (n_p, T_p), doubly charged alpha particles, He^{++} (n_i, T_i), electron beam (n_b, T_b, U_b) streaming along ambient magnetic field and superthermal electrons (n_e, T_e) following kappa distribution. The electrostatic waves are propagating obliquely in the x-z plane making an angle θ to the ambient magnetic field $\mathbf{B}_0$ which is considered to be in $z-$direction. The dynamics of electrostatic plasma waves is governed by the following fluid equations:

$$\frac{\partial n_s}{\partial t} + \nabla.(n_s\mathbf{v}_s) = 0 \tag{1}$$

$$m_s n_s\left[\frac{\partial \mathbf{v}_s}{\partial t} + (\mathbf{v}_s.\nabla)\mathbf{v}_s\right] = q_s n_s(\mathbf{E} + \mathbf{v}_s \times \mathbf{B}_0) - \nabla P_s \tag{2}$$

Here, n_s, $\mathbf{v}_s$, m_s, q_s, P_s, represent respectively, density, velocity, mass, charge and pressure of the individual species 's', which stands for protons (p), doubly charged Helium ions (i), and beam electrons (b). The pressure term is $\nabla P_s = \gamma_s T_s \nabla n_s$, where γ_s is the ratio of specific heats and T_s represent the temperature of each species.

The superthermal electrons are assumed to follow kappa distribution [37, 38] given by:

$$f_\kappa(v) = \frac{n_{e0}}{\pi^{\frac{3}{2}}}\frac{1}{\theta_\kappa{}^3}\frac{\Gamma(\kappa+1)}{\kappa^{\frac{3}{2}}\Gamma\left(\kappa-\frac{1}{2}\right)}\left(1+\frac{v^2}{\kappa\theta_\kappa{}^2}\right)^{-(\kappa+1)} \tag{3}$$

where $\theta_\kappa = \sqrt{\left[\frac{2\kappa-3}{\kappa}\right]\left(\frac{T_e}{m_e}\right)}$ is the modified thermal speed and κ is the superthermality index with $\kappa > 3/2$.

The number density of the kappa distributed electrons is found by integrating equation (3) in presence of electrostatic potential ϕ. This can be obtained by replacing v^2/θ_κ^2 by $v^2/\theta_\kappa^2 - 2e\phi/m_e\theta_\kappa^2$ [39, 40]:

$$n_e = n_{e0}\left[1 - \frac{e\phi}{T_e\left(\kappa - \frac{3}{2}\right)}\right]^{\frac{1}{2}-\kappa} \tag{4}$$

The perturbed number density of each individual fluid component (n_{p1}, n_{i1}, n_{b1}, n_{e1}) is obtained by linearizing the equation (1), (2) and (4). The general expression for the perturbed number density of s^{th} species 's'and kappa electrons (e) can be written as

$$n_{s1} = \frac{n_{s0}\left[k^2\sin^2\theta + k^2\cos^2\theta\left(1 - \frac{\Omega_s^2}{(\omega - \mathbf{k}.\mathbf{U}_{bs})^2}\right)\right]e\phi}{(\omega - \mathbf{k}.\mathbf{U}_{bs})^2 m_s\left(1 - \frac{\Omega_s^2}{(\omega - \mathbf{k}.\mathbf{U}_{bs})^2}\right) - \gamma_s T_s k^2\sin^2\theta - \gamma_s T_s k^2\cos^2\theta\left(1 - \frac{\Omega_s^2}{(\omega - \mathbf{k}.\mathbf{U}_{bs})^2}\right)} \tag{5}$$

and

$$n_{e1} = \left(\frac{2\kappa - 1}{2\kappa - 3}\right)n_{e0}\frac{e\phi}{T_e} \tag{6}$$

Here, $\mathbf{U}_{bs}$ represent velocity of beam. In our model, we are considering electron beam, hence $\mathbf{U}_{bs} \equiv \mathbf{U}_b$ and for all other species this term goes to zero, i.e., $\mathbf{U}_{bp,i,e} = 0$.

Substitution of perturbed densities in the following Poisson's equation

$$\nabla^2\phi = -\frac{e}{\epsilon_0}(n_{p1} + z_i n_{i1} - n_{b1} - n_{e1}) \tag{7}$$

and simplification yield the following dispersion relation:

$$\begin{aligned} 1 + \frac{\omega_{pe}^2}{k^2 v_{te}^2}\frac{2\kappa - 1}{2\kappa - 3} &= \frac{\omega_{pb}^2[(\omega - \mathbf{k}.\mathbf{U}_b)^2 - \Omega_b^2\cos^2\theta]}{(\omega - \mathbf{k}.\mathbf{U}_b)^4 - (\omega - \mathbf{k}.\mathbf{U}_b)^2\Omega_b^2 - \gamma_b k^2 v_{tb}^2[(\omega - \mathbf{k}.\mathbf{U}_b)^2 - \Omega_b^2\cos^2\theta]} \\ &+ \frac{\omega_{pp}^2[\omega^2 - \Omega_p^2\cos^2\theta]}{\omega^4 - \omega^2\Omega_p^2 - \gamma_p k^2 v_{tp}^2[\omega^2 - \Omega_p^2\cos^2\theta]} + \frac{\omega_{pi}^2[\omega^2 - \Omega_i^2\cos^2\theta]}{\omega^4 - \omega^2\Omega_i^2 - \gamma_i k^2 v_{ti}^2[\omega^2 - \Omega_i^2\cos^2\theta]} \end{aligned} \tag{8}$$

Here, $\omega_{ps} = \sqrt{\frac{n_{s0}z_s^2 q_s^2}{\epsilon_0 m_s}}$, $\Omega_s = \frac{z_s q_s B_0}{m_s}$ and $v_{ts} = \sqrt{\frac{T_s}{m_s}}$ are, respectively, the plasma frequency, cyclotron frequency and thermal velocity of s^{th} species with z_s being the charge state of the plasma species and n_{s0} being the unperturbed number density. Except for Helium ions, all other plasma species are singly charged, i.e., $z_{p,b,e} = 1$ and for Helium, z_i will be 2. The term $\omega - \mathbf{k}.\mathbf{U}_b$ plays a central role in the generating the non-resonant instability in the system. The Landau resonance occurs at $\omega \sim \mathbf{k}.\mathbf{U}_b$ and the term containing $\omega - \mathbf{k}.\mathbf{U}_b$ in the denominator becomes very large (going to infinity) at exact resonance. However, in the present work, we avoid the Landau resonance which requires a kinetic treatment.

In the absence of ambient magnetic field, the dispersion relation reduces to equation (6) of Sreeraj *et al* [27] for an unmagnetized plasma. If the number density of beam electrons in equation (8) is taken to be zero ($n_{b0} = 0$), one arrives at dispersion relation for electrostatic waves derived by Sreeraj *et al* [41] for oblique propagation (their equation (6)).

For parallel propagation (i.e. for $\theta = 0°$), equation (8) becomes:

$$\begin{aligned} &((\omega - kU_b)^2 - \Omega_b^2)(\omega^2 - \Omega_p^2)(\omega^2 - \Omega_i^2) \\ &\left[1 - \frac{\omega_{pb}^2}{\left(1 + \frac{\omega_{pe}^2}{k^2 v_{te}^2}\frac{2\kappa - 1}{2\kappa - 3}\right)((\omega - kU_b)^2 - \gamma_b k^2 v_{tb}^2)} - \frac{\omega_{pp}^2}{\left(1 + \frac{\omega_{pe}^2}{k^2 v_{te}^2}\frac{2\kappa - 1}{2\kappa - 3}\right)(\omega^2 - \gamma_p k^2 v_{tp}^2)} - \frac{\omega_{pi}^2}{\left(1 + \frac{\omega_{pe}^2}{k^2 v_{te}^2}\frac{2\kappa - 1}{2\kappa - 3}\right)(\omega^2 - \gamma_i k^2 v_{ti}^2)}\right] = 0 \end{aligned} \tag{9}$$

In this case decoupling of cyclotron and acoustic modes occurs, i.e., the electron cyclotron ($\omega = kU_b \pm \Omega_b$), proton cyclotron ($\omega = \pm\Omega_p$) and Helium cyclotron modes ($\omega = \pm\Omega_i$) decouple from the acoustic modes given by the expressions in square brackets in equation (9) (which are same as represented by Eqn (6) of Sreeraj *et al* [27]). It also has to be emphasized that proton and helium cyclotron modes are non-propagating modes whereas electron cyclotron mode propagates.

For electrostatic waves propagating perpendicular ($\theta = 90°$) to the ambient magnetic field, dispersion relation can be written as:

$$\left[1 - \frac{\omega_{pb}^2}{\left(1 + \frac{\omega_{pe}^2}{k^2 v_{te}^2}\frac{2\kappa - 1}{2\kappa - 3}\right)(\omega^2 - \Omega_b^2 - \gamma_b k^2 v_{tb}^2)} - \frac{\omega_{pp}^2}{\left(1 + \frac{\omega_{pe}^2}{k^2 v_{te}^2}\frac{2\kappa - 1}{2\kappa - 3}\right)(\omega^2 - \Omega_p^2 - \gamma_p k^2 v_{tp}^2)} - \frac{\omega_{pi}^2}{\left(1 + \frac{\omega_{pe}^2}{k^2 v_{te}^2}\frac{2\kappa - 1}{2\kappa - 3}\right)(\omega^2 - \Omega_i^2 - \gamma_i k^2 v_{ti}^2)}\right] = 0 \tag{10}$$

Further, in the absence of electron beam ($n_{b0} = 0$), one arrive at dispersion relation for electrostatic waves derived by Sreeraj *et al* [41] (cf equation (18)). In the section 3, the dispersion relation (equation (8)) is solved numerically for various plasma modes for relevant plasma parameters.

3. Numerical analysis

In this section, the numerical analysis of dispersion relation equation (8) is carried out. The relevant plasma parameters are taken from Tao *et al* [25] and Mangeney *et al* [42]. The various plasma parameters are normalized as follows: the frequencies are normalized with electron plasma frequency, $\omega_{pe} = \sqrt{\frac{n_{e0}e^2}{\epsilon_0 m_e}}$; wave number k by Debye length of electron, $\lambda_{De} = \sqrt{\frac{\epsilon_0 T_e}{n_{e0}e^2}} = \frac{v_{te}}{\omega_{pe}}$. The beam velocity is normalized with ion-acoustic velocity, $c_s = \sqrt{\frac{T_e}{m_p}}$. The number densities of the species is bound by the quasi neutrality condition, $n_{p0} + z_i n_{i0} = n_{b0} + n_{e0}$. The values of γ_s are taken to be the same, i.e. $\gamma_b = \gamma_i = \gamma_p = 3 = \gamma$. One can use either the exact plasma parameters or normalized ones. The benefit of using the normalized parameters for numerical study is that one does not have to worry about the dimensions and it will ease the computations. One can easily convert the normalised parameters to actual values for interpretation of the results.

We have divided the subsections in this order: in section 3.1, equation (8) is analyzed for parallel propagation, $\theta = 0°$ and varying the beam velocity. This will show the merging of different plasma modes. In section 3.2, the dispersion relation equation (8) is investigated numerically for different angles of propagation with the velocity of electron beam set to zero, i.e. $U_b = 0$. This will bring out the coupling of various plasma modes. Finally, in section 3.3, equation (8) is investigated numerically for different angles of propagation with the finite beam velocity. Since, we are dealing with the fluid approach, both Landau and cyclotron dampings will not have any bearing on our results.

3.1. Effect of electron beam variation

Here, the general dispersion relation is analyzed for different values of electron beam velocity for the case of parallel ($\theta = 0°$) propagation. In figure 1(a), dispersion curves corresponding to equation (8) are plotted with $k\lambda_{De}$ on x-axis and $\frac{\omega_r}{\omega_{pe}}$ on y-axis. The number densities are normalized with respect to total number density of electrons and temperature by temperature of kappa electron. The total number density is given by the expression $N_0 = n_{e0} + n_{b0} = n_{p0} + z_i\, n_{i0}$. The parameters fixed for this set of variation are $n_{b0}/N_0 = 0.01$, $n_{i0}/N_0 = 0.05$, $\kappa = 6$, $T_b/T_e = 0.002\,5$, $T_p/T_e = 0.2$, $T_i/T_e = 0.4$, $\gamma = 3$, $\omega_{pp}/\Omega_p = 1620$ and $\theta = 0°$. Numerical analysis of the dispersion relation shows the presence of 12 modes in the plasma which are identified by colored lines in figures 1(a), (b) and in subsequent figures. These are electron cyclotron modes (1 [dashed line- green colored] and 12 [long dashed line- baby blue colored]), electron acoustic modes (2 [solid line- black colored] and 11 [short dashed line- blue colored]), fast ion acoustic modes (3 [dash dotted line- red colored] and 10 [medium dashed line- majestic purple colored]) and slow ion acoustic modes (4 [dash dot dotted line- magenta colored] and 9 [extra long dashed line- cyan colored]) (see figure 1(a)). The other four modes are shown in figure 1(b) due to scaling. They are proton cyclotron mode (5 [dash dot dot dotted line- sea green colored] and 8 [dash dash dot dot dotted line- yellow colored]) and Helium cyclotron mode (6 [dash dash dotted line- spring green colored] and 7 [dash dash dot dotted line- pink colored]). In Sreeraj *et al* [27], we have outlined the procedure to identify the different plasma modes. For $\theta = 0°$ and $\frac{U_b}{c_s} = 0$ (figures 1(a) and 1b), proton, Helium and electron cyclotron modes are non-propagating modes, i. e., they represent oscillations at their respective cyclotron frequencies. The acoustic and cyclotron modes de-couple at $\theta = 0°$. Modes 1–6 have positive phase speeds, whereas modes 7–12 have negative phase speeds. All the acoustic modes start with frequency $\frac{\omega_r}{\omega_{pe}} = 0$ at $k\lambda_{De} = 0$, on the other hand, electron, proton and Helium cyclotron modes start at their respective cyclotron frequencies, i.e., at $\omega_r/\omega_{pe} = 2.647\,5 \times 10^{-2}$, 1.4×10^{-5} and 7×10^{-6}, respectively as shown in figures 1(a), (b). This figure is similar to figure 1(a) of Sreeraj *et al* [27], except for the fact that here additional modes, i.e., electron and ion cyclotron modes appear.

It is interesting to note that though the phase speed of all modes gets affected with the increase in electron beam velocity, it is the mode 11 which shows appreciable change in its phase speed and crosses over that of the modes 9 and 10. When the beam velocity is increased to $\frac{U_b}{c_s} = 4$ (figure 1(c)), the electron acoustic mode (mode 11), which had a negative phase speed initially (see figure 1(a)), starts to become positive at $k\lambda_{De} \geqslant 2.33$ (for variations in between, kindly see Sreeraj *et al* [27]) and has large phase speed than modes 9 and 10. The striking feature that differentiates this figure from figure 1(c) in the Sreeraj *et al* [27] is the behavior of modes 1 and 12 (electron cyclotron modes). For parallel propagation and $\frac{U_b}{c_s} = 0$, the electron, proton and Helium cyclotron modes will have a constant frequency for all the values of $k\lambda_{De}$. However, the introduction of electron beam velocity brings in ($\omega - \mathbf{k}.\mathbf{U}_b$) term, which modifies these modes significantly. The mode 11 gains the free energy from the electron beam and increases the phase velocity.

The dispersion curves show an interesting pattern at $\frac{U_b}{c_s} = 4.4$. The phase velocity of electron acoustic mode (mode 11) attains a positive value at $k\lambda_{De} \geqslant 0.64$, and merges with the slow ion acoustic mode (mode 4) and electron beam drives slow ion acoustic mode in the $k\lambda_{De}$ range of 2.97–4.24 (see figure 1(d)). In this region phase velocity of mode 11 (electron acoustic mode) and mode 4 (slow ion acoustic mode) are the same with finite imaginary part which corresponds to finite growth rate and is shown in the lower panel of figure 1(d). The maximum growth has a value of $\frac{\omega_i}{\omega_{pe}} = 1.77 \times 10^{-3}$ which occurs at $k\lambda_{De} = 3.59$ and corresponding real frequency, $\frac{\omega_r}{\omega_{pe}} = 4.815 \times 10^{-2}$. For some values of $k\lambda_{De}$, the solution of equation (8) gives complex conjugate roots. This implies that those two modes will have same phase speeds and hence, merge together to form an

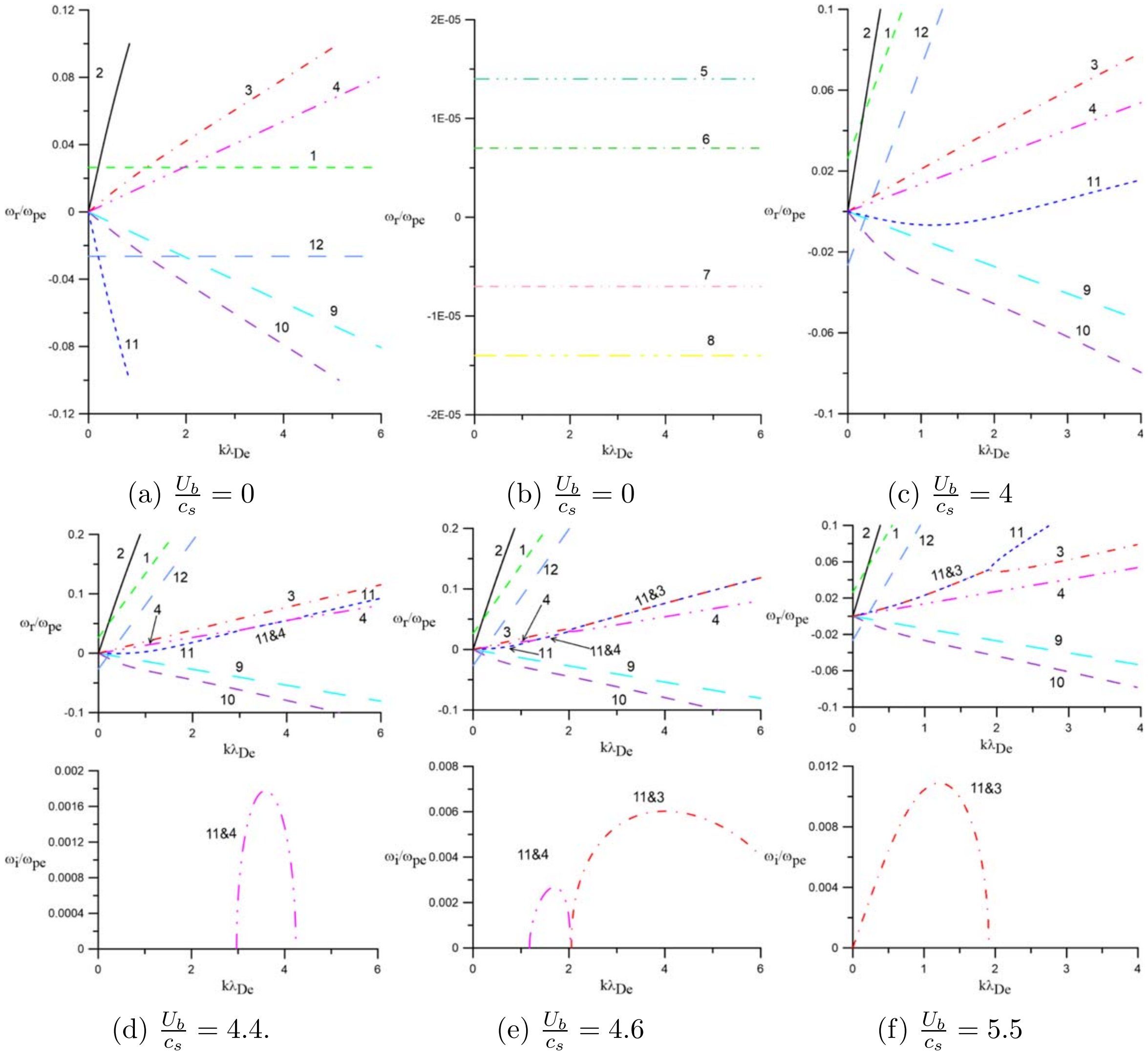

(a) $\frac{U_b}{c_s} = 0$ (b) $\frac{U_b}{c_s} = 0$ (c) $\frac{U_b}{c_s} = 4$

(d) $\frac{U_b}{c_s} = 4.4.$ (e) $\frac{U_b}{c_s} = 4.6$ (f) $\frac{U_b}{c_s} = 5.5$

Figure 1. Dispersion curves for various values of $\frac{U_b}{c_s}$, with fixed plasma parameters: $\theta = 0°$, $n_{b0}/N_0 = 0.01$, $n_{i0}/N_0 = 0.05$, $\kappa = 6$, $T_b/T_e = 0.002\,5$, $T_p/T_e = 0.2$, $T_i/T_e = 0.4$. Various lines indicate different plasma modes: in figure 1(a), electron cyclotron modes 1 and 12 (dashed line[green colored] and long dashed line [baby blue colored] respectively); electron acoustic modes 2 and 11 (solid line [black colored] and short dashed line [blue colored] respectively); fast ion acoustic modes 3 and 10 (dash dotted line [red colored] and medium dashed line [majestic purple colored] respectively); slow ion acoustic modes 4 and 9 (dash dot dotted line [magenta colored] and extra long dashed line [cyan colored] respectively) and in figure 1(b), proton cyclotron modes 5 and 8 (dash dot dot dotted line [sea green colored] and dash dash dot dot dotted line [yellow colored] respectively); and helium cyclotron modes 6 and 7 (dash dash dotted line [spring green colored] and dash dash dot dotted line [pink colored] respectively). In figures 1(d)–(f), upper and lower panels show the real frequency (ω_r/ω_{pe}) and growth rates (ω_i/ω_{pe}), respectively, which arises due to merging of different modes, whereas, no merging occurs at $\frac{U_b}{c_s} = 4$ (figure 1(c)).

unstable region. With further increase in the beam velocity to $\frac{U_b}{c_s} = 4.6$ (see figure 1(e)), it is seen that merging of acoustic modes happens at two different places: in the lower $k\lambda_{De}$ range (between 1.18–2.03), electron acoustic mode (mode 11) merges with slow ion acoustic mode (mode 4) to form electron beam driven slow ion acoustic mode and in the higher $k\lambda_{De}$ range (between 2.05–6.81) forms electron beam driven fast ion acoustic mode by merging with fast ion acoustic mode (mode 3). Electron beam driven slow ion acoustic mode exists in shorter $k\lambda_{De}$ range compared to electron beam driven fast ion acoustic mode. There exist a small $k\lambda_{De}$ range wherein mode 11 does not interact with any other mode. The maximum growth rate of beam driven slow ion acoustic mode ($\frac{\omega_i}{\omega_{pe}} \approx 2.68 \times 10^{-3}$) is smaller than that of fast ion acoustic mode ($\frac{\omega_i}{\omega_{pe}} \approx 6.02 \times 10^{-3}$). However, fast ion acoustic mode is unstable for larger wave-number range as compared to slow ion acoustic mode.

The merging of mode 11 continues with slow and fast ion-acoustic modes with increase in electron beam velocity until $\frac{U_b}{c_s} < 5.5$ with electron beam driven fast ion-acoustic mode having larger growth rate than the slow ion-acoustic mode. For $5.5 \leqslant \frac{U_b}{c_s} < 7.8$, only electron beam driven fast ion acoustic mode exist with decreasing growth rate and beyond $U_b/cs \geqslant 7.8$, there are no unstable modes. These results are consistent with four-component unmagnetized model of Sreeraj *et al* [27].

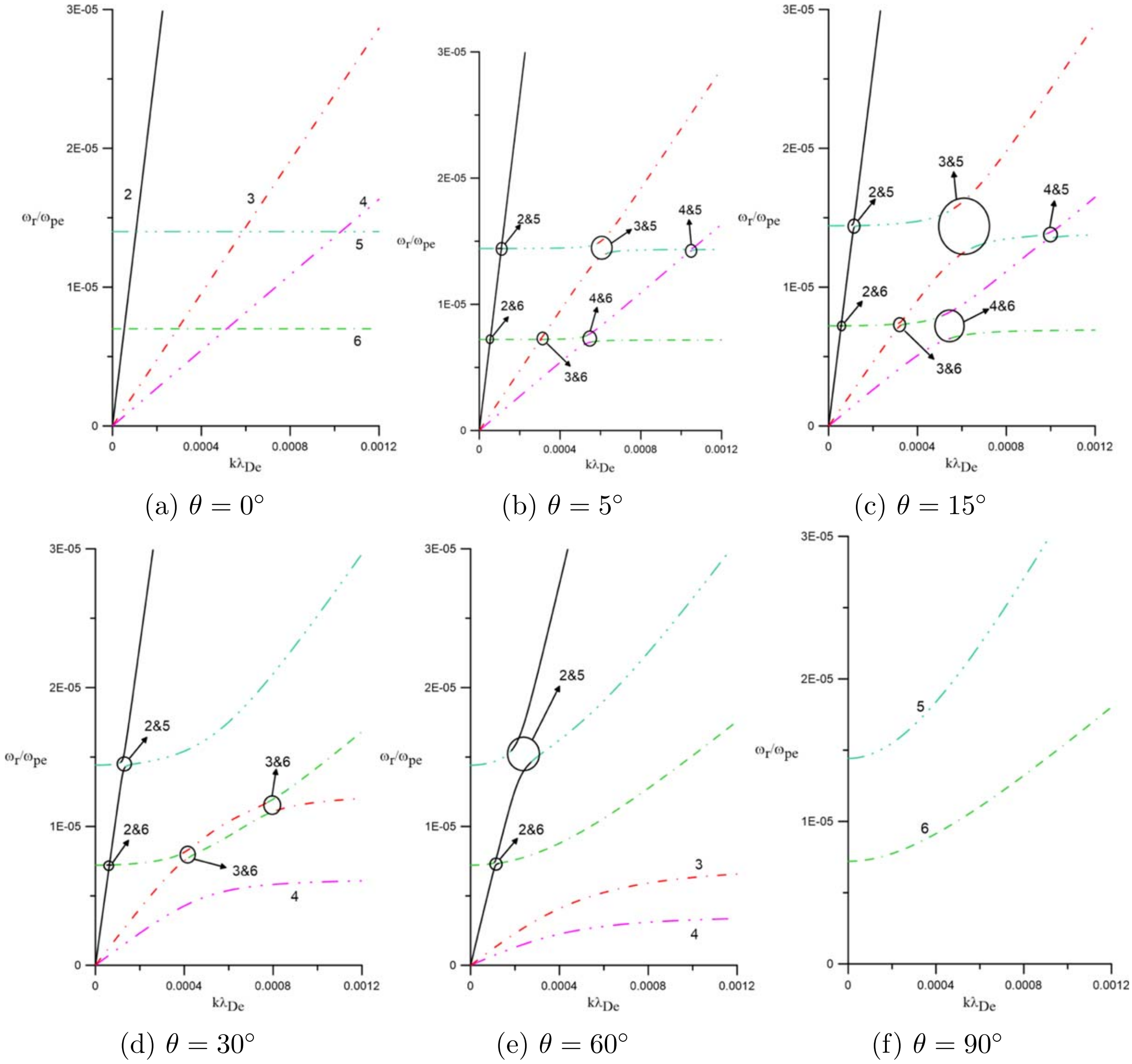

Figure 2. Effect of angle of propagation, θ, on the strength of coupling between different modes for $U_b/c_s = 0$. Other plasma parameters are the same as in figure 1.

3.2. Effect of variation of angle of propagation without electron beam streaming

In this section, we discuss the effect of obliqueness on the dispersion relation equation (8) without electron beam streaming. This is an extension of theoretical analysis carried out in [41] for the case of coupling of electrostatic ion cyclotron and acoustic modes in the solar wind plasma, wherein the magnetized plasma comprised of kappa electron, fluid proton and doubly charged Helium ions. The numerical analysis shows that there is no change in the dispersion characteristic of electron cyclotron mode in the $k\lambda_{De}$ range considered, hence we have omitted it in the dispersion relation plots to represent other modes clearly.

For $\theta = 0°$, all the modes are decoupled as shown in figure 2(a). Modes 5 and 6 represent the proton and Helium cyclotron modes, respectively. In the case of parallel propagation, these modes are non-propagating modes and the only physically acceptable solution are that of acoustic modes. It has to be emphasized that similar kind of plots exist with negative phase speed, but in-order to show the dispersion relation plots clearly, we have shown only those with positive phase speed. When finite angle of propagation is introduced ($\theta = 5°$), the coupling of different modes can be seen clearly in figure 2(b). Circles indicate the occurrence of coupling various modes. The mode 2 couples with modes 6 and 5 at $k\lambda_{De}$ value of 6×10^{-5} and 1.3×10^{-4}, respectively. Similarly, mode 3 couples with mode 6 at $k\lambda_{De} \approx 3.1 \times 10^{-4}$. Mode 4 couples with mode 6 in the $k\lambda_{De}$ range $5 \times 10^{-4} - 6 \times 10^{-4}$, mode 3 couples with mode 5 in the $k\lambda_{De}$ range $5.5 \times 10^{-4} - 6.8 \times 10^{-4}$ and mode 4 couples with mode 5 in the $k\lambda_{De}$ range $1.03 \times 10^{-3} - 1.07 \times 10^{-3}$. Taking into consideration, the couplings between the modes with negative phase speed, in total the coupling happens at 12 different places (different wave numbers), which is in sharp contrast to what is shown in Sreeraj *et al* [41], where coupling occurred at 8 different places.

With the angle of propagation increased to 15° as shown in figure 2(c), it is clear from dispersion curve that the coupling between modes 3 and 5 is much weaker compared to that in case of figure 2(b). This is indicated by the gap between the modes. The coupling between modes 2 and 6 remains the strongest one which is happening at $k\lambda_{De} \approx 6 \times 10^{-5}$. There exist a certain $k\lambda_{De}$ range in which other modes couple: mode 4 couples with mode 6 in the range $k\lambda_{De} \approx 5 \times 10^{-4} - 6.5 \times 10^{-4}$; mode 4 couples with mode 5 in $k\lambda_{De} \approx 9.65 \times 10^{-4} - 1.04 \times 10^{-3}$; mode 3 couples with mode 6 in $k\lambda_{De} \approx 2.9 \times 10^{-4} - 3.5 \times 10^{-4}$; mode 3 couples with mode 5 in $k\lambda_{De} \approx 5.3 \times 10^{-4} - 7.5 \times 10^{-4}$; mode 2 and mode 5 in $k\lambda_{De} \approx 9 \times 10^{-5} - 1.4 \times 10^{-4}$.

The coupling between modes 3 and 5, 4 and 5 and 4 and 6 vanishes when the angle of propagation is increased to 30° (see figure 2(d)). Here, mode 3 couples with mode 6 in two different $k\lambda_{De}$ regime: first in $3.8 \times 10^{-4} - 4.4 \times 10^{-4}$ and then at $7.6 \times 10^{-4} - 8.4 \times 10^{-4}$. Furthermore, the coupling between mode 2 and mode 6 still remains intact and occurs at $k\lambda_{De} \approx 7 \times 10^{-5}$. However, the coupling between modes 2 and 5 is weak as compared to that in case of $\theta = 15°$ (see figure 2(c)) and occurs in the $k\lambda_{De}$ range $9 \times 10^{-5} - 1.5 \times 10^{-4}$. The slow ion acoustic mode (mode 4) completely decouples from the rest of the modes.

For $\theta = 60°$ and $\frac{U_b}{c_s} = 0$, the dispersion relation curves is shown in figure 2(e). It is seen that the mode 3 (fast ion acoustic) and mode 4 (slow ion acoustic) do not couple with any of the cyclotron modes. The only coupling is between mode 2 and mode 6 at $k\lambda_{De} \approx 7\times10^{-5}$ and then between mode 2 and mode 5 in the $k\lambda_{De}$ range $1 \times 10^{-4} - 1.8 \times 10^{-4}$. Further increasing the angle of propagation weakens the coupling between mode 2 and mode 5.

The coupling between modes 2 and 5 vanishes when angle of propagation reaches 80° (not shown here) and the only coupling that exist is between modes 2 and 6. A notable thing to mention here is that the frequencies of slow and fast ion acoustic mode decrease substantially compared to that of figure 2(e). Finally for $\theta = 90°$, the only cyclotron mode exist in the system as seen in figure 2(f).

It must be emphasized here that coupling of mode 2 with modes 5 and 6 appears to be much stronger than the coupling of mode 3 with modes 5 and 6 and coupling of mode 4 with modes 5 and 6. Among all the modes, the coupling between modes 2 and 6 is the strongest whereas the weakest coupling occurs between modes 3 and 5. The coupling between modes 2 and 6 continues to exist for highly oblique angle of propagation.

3.3. Effect of variation of angle of propagation with finite electron beam streaming

In this section, dispersion relation equation (8) is analyzed for various angles of propagation with normalized electron beam velocity fixed at 4.5. Please note that in figures 4, 5, the left and right hand panels exclusively show the coupling and merging of the modes, respectively.

In figure 3(a) for an angle of propagation $\theta = 5°$, it can be seen that the coupling happening at 6 different places between the modes with positive phase speeds and 4 different places with

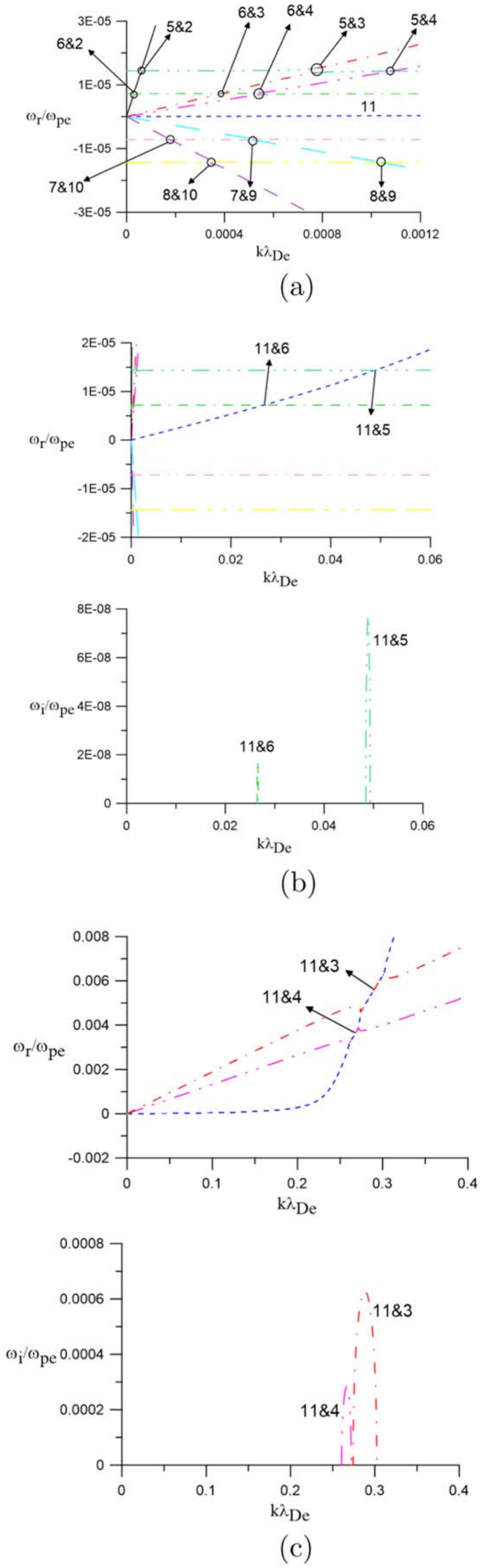

Figure 3. Plots showing coupling (figure 3(a)) and merging (figures 3(b), (c)) of different modes for $\theta = 5°$ and $U_b/c_s = 4.5$ in different $k\lambda_{De}$ range. Other plasma parameters are the same as in figure 1.

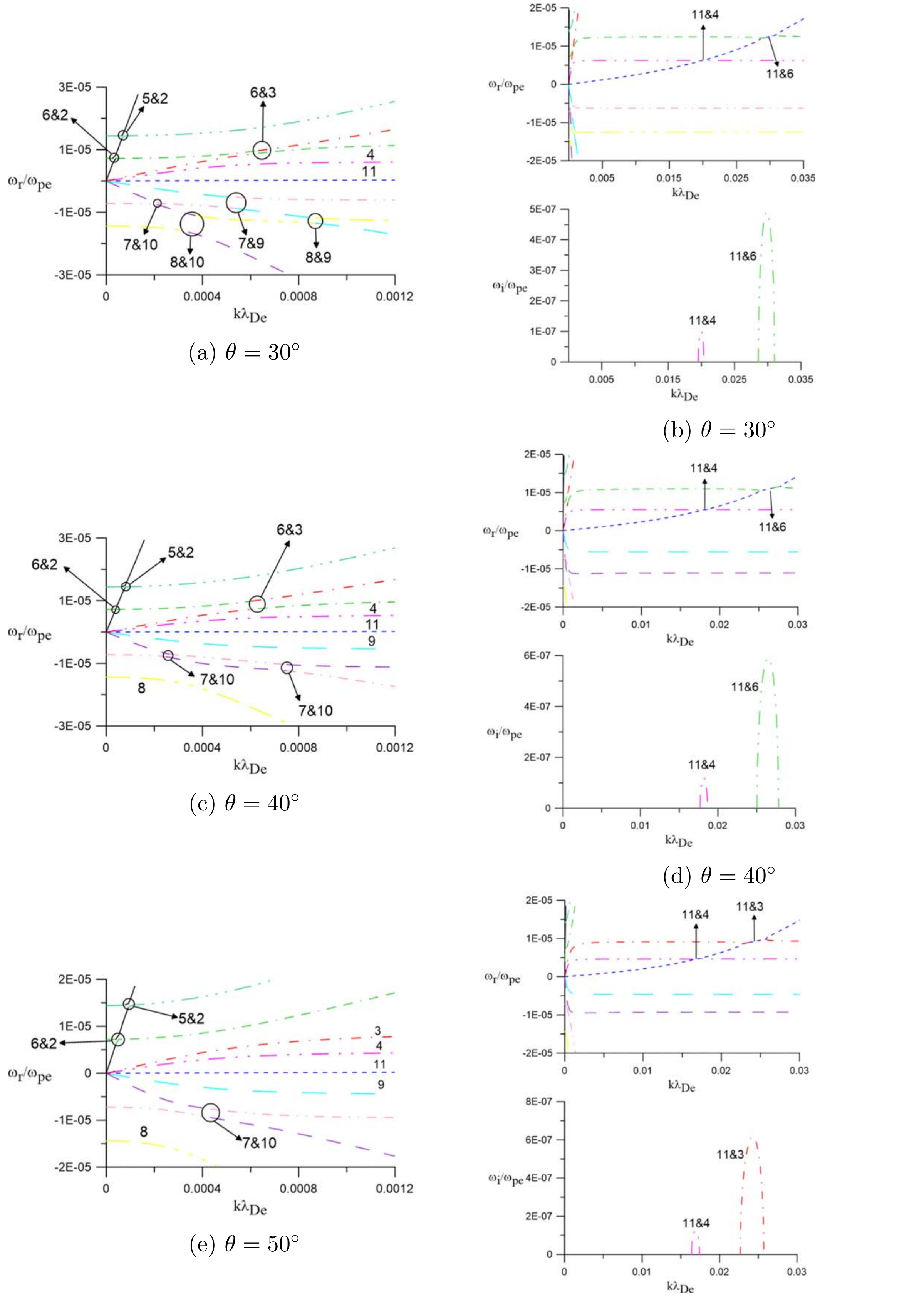

(a) $\theta = 30^{\circ}$

(b) $\theta = 30^{\circ}$

(c) $\theta = 40^{\circ}$

(d) $\theta = 40^{\circ}$

(e) $\theta = 50^{\circ}$

(f) $\theta = 50^{\circ}$

Figure 4. Plots showing coupling (figures 4(a), (c), (e)) and merging (figures 4(b), (d), (f)) of different modes for $\theta = 30^{\circ}$, $\theta = 40^{\circ}$ and $\theta = 50^{\circ}$, respectively with $U_b/c_s = 4.5$. Other plasma parameters are the same as in figure 1.

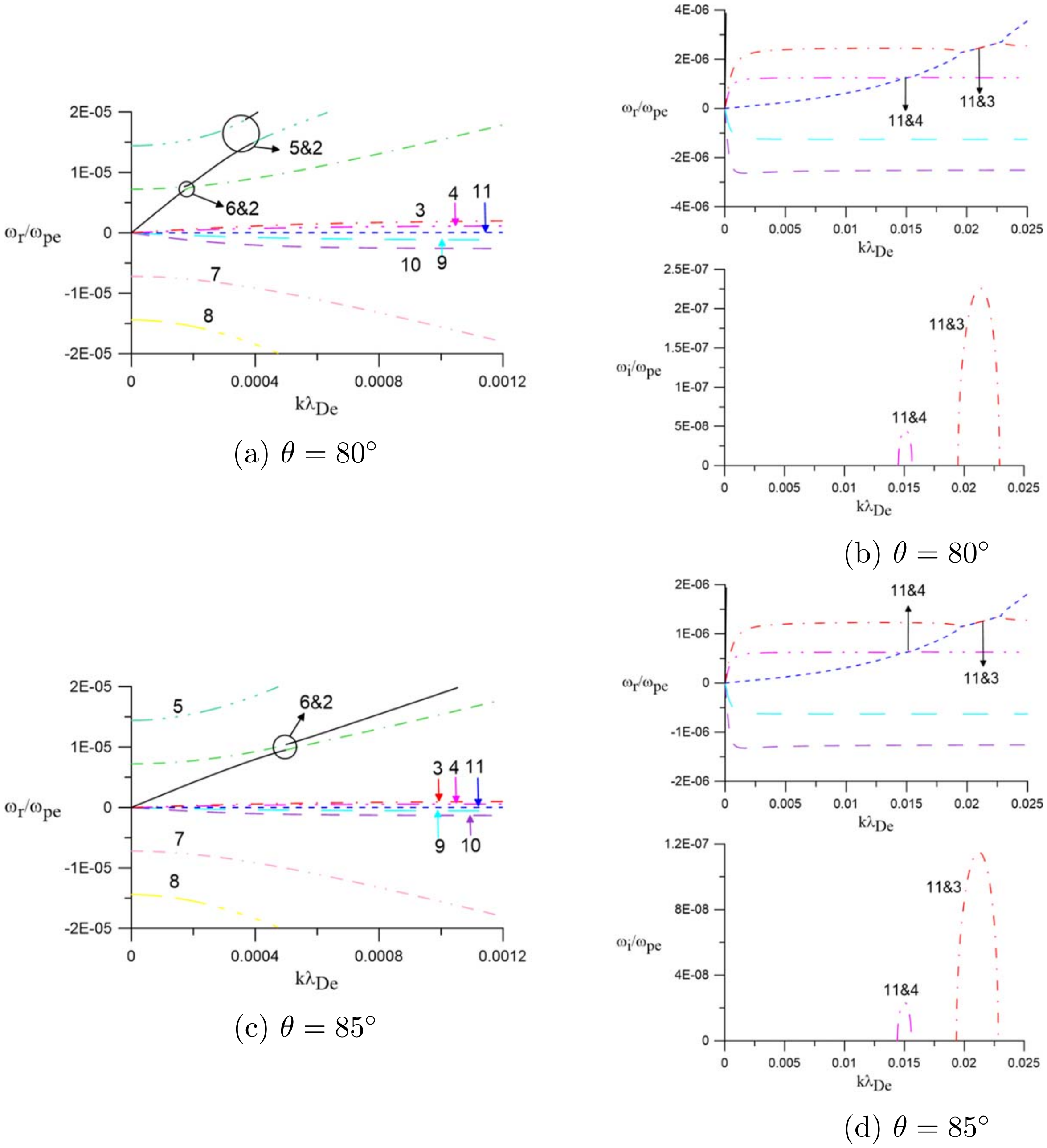

Figure 5. Plots showing coupling (figures 5(a), (c)) and merging (figures 5(b), (d)) of different modes for $\theta = 80°$ and $\theta = 85°$ with $U_b/c_s = 4.5$. Other plasma parameters are the same as in figure 1.

negative phase speeds. This is in sharp contrast to what was reported for in section 3.2, where equal number of couplings were observed between the modes with positive and negative phase speeds. Figure 3(b) shows the same dispersion plot as in figure 3(a), but in the higher $k\lambda_{De}$ range. Here, one can clearly see the merging of mode 11 with mode 6 thereby generating a unstable region first in the $k\lambda_{De}$ range $2.64 \times 10^{-2} - 2.67 \times 10^{-2}$ (which is electron beam driven Helium cyclotron mode) with maximum growth rate 1.74×10^{-8} and then between mode 11 and 5 in $k\lambda_{De}$ range $4.85 \times 10^{-2} - 4.93 \times 10^{-2}$ (which is electron beam driven proton cyclotron mode) with maximum growth rate 7.67×10^{-8}. Thus, the proton and helium cyclotron modes are excited by an electron beam. When $k\lambda_{De}$ range is increased further, we see merging of wave modes first for $k\lambda_{De} \approx 0.2605 - 0.2718$ with maximum growth rate occurring at $k\lambda_{De} \approx 0.2666$ with $\frac{\omega_r}{\omega_{pe}} \approx 3.54 \times 10^{-3}$ and $\frac{\omega_i}{\omega_{pe}} \approx 2.8 \times 10^{-4}$ (figure 3(c)). This can be identified as merging between modes 11 and 4. The second merging happens for $k\lambda_{De} \approx 0.2741 - 0.3024$ with maximum growth rate occurring at $k\lambda_{De} \approx 0.2881$ with $\frac{\omega_r}{\omega_{pe}} \approx 5.48 \times 10^{-3}$ and $\frac{\omega_i}{\omega_{pe}} \approx 6.3 \times 10^{-4}$. This is the merging of modes 11 and 3 (see figure 3(c)). The wavelengths corresponding to slow (mode 4) and fast (mode 3) ion acoustic modes are found to be $\approx$1178 m and 1090 m, respectively for electron Debye length of 50 m [25]. The Larmor radius of proton, Helium, electron and beam electrons is ≈36229 m, 51236 m, 1890 m, and 94 m, respectively. For clarity, we have only shown the merged modes in figure 3(c) and other modes have been omitted. With further increase in angle of propagation to 10° (not shown here), mode 11 still merges with mode 6 in $k\lambda_{De}$ range $2.51 \times 10^{-2} - 2.55 \times 10^{-2}$ with maximum growth rate 3.51×10^{-8} and then with mode 5 in the $k\lambda_{De}$ range $4.29 \times 10^{-2} - 4.43 \times 10^{-2}$ with maximum growth rate 1.61×10^{-7}.

The dispersion relation curves for $\theta = 30°$ are shown in figures 4(a), (b). It is clear from figure 4(a), the mode 4 does not couple with any other modes. It is noticed that all the coupling regions for wave modes with negative phase speeds come closer to each other and shift towards the lower wave number regime. In figure 4(b), the mode 11 first merges with mode 4 in the $k\lambda_{De}$ range $1.95 \times 10^{-2} - 2.04 \times 10^{-2}$ generating electron beam driven slow-ion acoustic mode with maximum growth rate 1.01×10^{-7} and then with mode 6 generating beam driven proton cyclotron mode in the $k\lambda_{De}$ range $2.86 \times 10^{-2} - 3.10 \times 10^{-2}$ with maximum growth rate of 4.91×10^{-7}. The growth rate of merged mode of 11 and 6 increases as compared to that of $\theta = 5°$ (as shown in figure 3(b)) and those of 10° (not shown here). For $\theta = 40°$, the coupling between all other modes with negative phase speed disappears except modes 7 and 10 which occurs at two different wave number ranges. On the other hand coupling between modes 3 and 6 and the coupling of mode 2 with modes 5 and 6 still exist (see figure 4(c)). The electron beam drives the modes 4 and 6 with higher growth rates (see figure 4(d)).

The coupling of mode 2 with modes 5 and 6 continue to exist for an angle of propagation $50^0 \leqslant \theta \leqslant 80^0$ with diminishing strength whereas the coupling between modes 7 and 10 disappears for $\theta > 50^0$ (figures 4(e), 5(a)). Further, there is no coupling between the modes for $\theta = 85°$ except between modes 2 and 6 which also vanishes at $\theta \geqslant 87°$ (not shown here). The modes that now merges with mode 11 are mode 4 in $k\lambda_{De}$ range $1.64 \times 10^{-2} - 1.74 \times 10^{-2}$ generating electron beam driven slow-ion acoustic mode with maximum growth rate to be 1.25×10^{-7} and mode 3 generating electron beam driven fast-ion acoustic mode in the $k\lambda_{De}$ range $2.27 \times 10^{-2} - 2.57 \times 10^{-2}$ with maximum growth rate to be 6.16×10^{-7} (see 4(f)). With further increase in the angle of propagation (figure 5(b) ($\theta = 80^0$) and figure 5(d) ($\theta = 85^0$)) mode 11 still merges with mode 4 and then with 3 driving slow and fast ion acoustic modes respectively with decreasing growth rates and unstable regions shifting to lower $k\lambda_{De}$ range. This trend continues till $\theta \leqslant 87°$.

For perpendicular propagation, the acoustic modes vanish and only proton, Helium and electron cyclotron modes exist similar to as seen in figure 2(f) (due to scaling electron cyclotron mode could not be shown) and their counter part with negative phase speed. At perpendicular propagation there will not be any unstable region as $\mathbf{k}.\mathbf{U}_b = 0$, hence, there is no source of free energy to excite the waves as seen in equation (8).

4. Conclusion

The propagation characteristics of linear electrostatic waves in a four-component magnetized plasma comprising of fluid protons, doubly charged fluid Helium ions, beam electron streaming along ambient magnetic field and superthermal electrons with kappa distribution are presented. The numerical analysis of the dispersion relation shows the presence of electron, proton and Helium cyclotron modes, slow and fast ion acoustic, and electron acoustic modes. For parallel propagation without electron streaming, the dispersion relation curves are perfectly symmetrical about x-axis (i.e., wavenumber axis). With increase in the electron beam velocity for parallel propagation, phase speed of electron acoustic mode turns to positive from initially negative value. The merging of the modes leads to unstable wave number regions with finite wave growth rate. The electron beam drives the slow ion acoustic mode in the lower wave-number regime and the fast ion acoustic mode in the higher wave-number regime.

The dispersion relation is further analysed for non- parallel propagation by keeping velocity of beam electron to zero revealing coupling of various modes in the plasma. It is seen coupling occurs at 12 different places- 6 among the modes with positive phase speeds and other 6 among the negative phase speeds. With increase in the angle of propagation, the coupling between the fast ion-acoustic (mode 3) and proton cyclotron (mode 5) is the first one to vanish followed by slow ion-acoustic (mode 4) and helium cyclotron (mode 6) and then slow ion-acoustic (mode 4) and proton cyclotron (mode 5) modes. The mode 3 couples with mode 6 at two different places at $\theta = 30°$ thereafter, it does not couple with any mode. Further increase in the angle of propagation decreases the strength of coupling between mode 2 (electron-acoustic) and mode 5 (proton cyclotron) compared to mode 2 (electron-acoustic) and mode 6 (Helium cyclotron). At perpendicular propagation, only cyclotron modes exist.

For oblique propagation with finite electron beam velocity, the coupling and merging of various modes occur. The coupling of wave modes occur for smaller wave numbers whereas the merging of wave modes is observed for higher wave numbers. For small angle of propagation coupling is seen in among large number of modes as compared to more oblique propagation. With increase in angle, coupling among the wave modes with negative phase speeds vanishes first followed by wave modes with positive phase speed. The strongest coupling occurs between electron acoustic and helium cyclotron modes which persist for nearly perpendicular propagation ($\theta \sim 85^0$). For angle of propagation $5^0 \leqslant \theta < 10^0$, electron beam drives the helium and proton cyclotron modes, for $30^0 \leqslant \theta < 40^0$, helium cyclotron and slow ion acoustic modes are driven unstable and for $50^0 \leqslant \theta < 85°$ slow as well as fast ion acoustic modes are excited. It is emphasized here that the coupling and merging of wave modes occur in the lower wave number range as compared to the cases without electron streaming and parallel propagation, respectively.

In unmagnetized plasma, only slow and fast ion acoustic modes were excited [27]. However, in magnetized plasma discussed here, the unique feature of the results is that proton as well as helium cyclotron modes are excited in addition to slow and fast ion acoustic modes. Further, growth rates as well as wave numbers of excited slow and fast ion acoustic modes are much smaller in magnetized plasma than the unmagnetized one. The wavelengths (growth rates) of slow and fast ion acoustic modes are smaller (larger) than the proton and helium cyclotron modes. The estimated frequencies of the ion-acoustic modes for the cases discussed here are $\omega \leqslant 0.01\omega_{pe}$ which corresponds to low-frequency waves observed by ARTEMIS Tao *et al* [25].

It is important to mention here that the scale lengths such as Larmor radius or Debye length play important role in the description of plasmas by MHD or kinetic theory. Fluid approach can be used in magnetized plasmas when Larmor radius is larger than the Debye length [36]. For the parameters considered here , the ratio of Larmor radius to Debye length comes out to be ≈1074, 760 and 40 for Helium ions, protons and electrons, respectively. Therefore, it is justified to use fluid theory in our model. However, more general kinetic theory is being developed which is beyond the scope of the present work.

Acknowledgments

GSL thanks the Indian National Science Academy (INSA) for the support under the INSA Honorary Scientist scheme.

References

[1] Ogilvie K W, Steinberg J T, Fitzenreiter R J, Owen C J, Lazarus A J, Farrell W M and Torbert R B 1996 *Geophys. Res. Lett.* **23** 1255–8
[2] Futaana Y, Barabash S, Wieser M, Holmström M, Bhardwaj A, Dhanya M B, Sridharan R, Wurz P, Schaufelberger A and Asamura K 2010 *J. Geophys. Res. Space* **115** A10248
[3] Dhanya M B, Bhardwaj A, Alok A, Futaana Y, Barabash S, Wieser M, Holmström M and Wurz P 2018 *Geophys. Res. Lett.* **45** 8826–33
[4] Dolginov S S, Eroshenko E G, Zhuzgov L N, Pushkov N V and Tyurmina L O 1961 *ARS J.* **31** 1640–4
[5] Dolginov S S, Yeroshenko E G, Zhuzgov L N and Pushkov N V 1963 *AIAA J.* **1** 514–6
[6] Ness N F 1965 *J. Geophys. Res.* **70** 517–34
[7] Michel F C 1968 *J. Geophys. Res.* **73** 7277–83
[8] Bosqued J M *et al* 1996 *Geophys. Res. Lett.* **23** 1259–62
[9] Bale S D, Owen C J, Bougeret J L, Goetz K, Kellogg P J, Lepping R P, Manning R and Monson S J 1997 *Geophys. Res. Lett.* **24** 1427–30
[10] Farrell W M, Kaiser M L and Steinberg J T 1997 *Geophys. Res. Lett.* **24** 1135–8
[11] Kellogg P J, Goetz K, Monson S J, Bougeret J L, Manning R and Kaiser M L 1996 *Geophys. Res. Lett.* **23** 1267–70
[12] Hashimoto K *et al* 2010 *Geophys. Res. Lett.* **37** L19204
[13] Borisov N and Mall U 2002 *J. Plasma Physics* **67** 277–99
[14] Rubia R, Singh S V and Lakhina G S 2016 *Phys. Plasmas* **23** 062902
[15] Rubia R, Singh S V and Lakhina G S 2018 *Phys. Plasmas* **25** 032302
[16] Lakhina G S and Singh S V 2015 *Sol. Phys.* **290** 3033–49
[17] Lakhina G S, Singh S V, Rubia R and Sreeraj T 2018 *Phys. Plasmas* **25** 080501
[18] Popel S I and Zelenyi L M 2013 *J. Plasma Physics* **79** 405–11
[19] Popel S I, Morfill G E, Shukla P K and Thomas H 2013 *J. Plasma Physics* **79** 1071–4
[20] Popel S I and Zelenyi L M 2014 *J. Plasma Physics* **80** 885–93
[21] Popel S I, Zelenyi L M and Atamaniuk B 2015 *Phys. Plasmas* **22** 123701
[22] Popel S I and Morozova T I 2017 *Plasma Phys. Rep.* **43** 566–75
[23] Wiehle S *et al* 2011 *Planet. Space Sci.* **59** 661–71
[24] Halekas J S *et al* 2011 *Space Sci. Rev.* **165** 93-107
[25] Tao J B *et al* 2012 *J. Geophys. Res. Space Physics* **117** A03106
[26] Rubia R, Singh S V and Lakhina G S 2017 *J. Geophys. Res. Space* **122** 9134-9147
[27] Sreeraj T, Singh S V and Lakhina G S 2018 *Phys. Plasmas* **25** 052902
[28] Olbert S 1968 *Summary of Experimental Results from M.I.T. Detector on IMP-1* (Netherlands: Springer)
[29] Vasyliunas V M 1968 *J. Geophys. Res.- Space* **73** 2839–84
[30] Livadiotis G and McComas D J 2013 *Space Sci. Rev.* **175** 183–214
[31] Livadiotis G 2015 *J. Geophys. Res.- Space* **120** 1607–19
[32] Halekas J S, Mitchell D L, Lin R P, Hood L L, Acuña M H and Binder A B 2002 *Geophys. Res. Lett.* **29** 77–1–77–4
[33] Halekas J S 2005 *J. Geophys. Res. Space* **110** A07222
[34] Halekas J S, Delory G T, Lin R P, Stubbs T J and Farrell W M 2008 *J. Geophys. Res. Space* **113** A09102
[35] Halekas J S, Poppe A R and McFadden J P 2014 *J. Geophys. Res. Space* **119** 5133–49
[36] Diver D A and Laing E W 2015 *Phys. Scr.* **90** 025602
[37] Mace R L and Hellberg M A 2009 *Phys. Plasmas* **16** 072113
[38] Pierrard V and Lazar M 2010 *Sol. Phys.* **267** 153–74
[39] Devanandhan S, Singh S V, Lakhina G S and Bharuthram R 2011 *Nonlinear Proc. Geoph.* **18** 627–34
[40] Devanandhan S, Singh S V, Lakhina G S and Bharuthram R 2012 *Phys. Plasmas* **19** 082314
[41] Sreeraj T, Singh S V and Lakhina G S 2016 *Phys. Plasmas* **23** 082901
[42] Mangeney A, Salem C, Lacombe C, Bougeret J L, Perche C, Manning R, Kellogg P J, Goetz K, Monson S J and Bosqued J M 1999 *Ann. Geophys.* **17** 307–20